International Journal of Geosynthetics and Ground Engineering (2023) 9:81
https://doi.org/10.1007/s40891-023-00499-y

ORIGINAL PAPER

Integrated Digital Image Analyses for Understanding the Particle Shape Effects on Sand–Geomembrane Interface Shear

Rizwan Khan[1] · **Gali Madhavi Latha**[1]

Received: 13 August 2023 / Accepted: 23 October 2023 / Published online: 6 November 2023

Abstract
This paper investigates the influence of particle shape on the multi-scale shear behavior of sand–geomembrane interfaces through advanced imaging techniques. Two sand specimens with similar particle size distribution but varying particle shapes were scanned using X-ray micro-computed tomography (μCT). The data were processed and analyzed using MATLAB to extract relevant shape parameters like sphericity, roundness, and fractal dimension. Interface shear tests were conducted using a modified direct shear apparatus, which allows image analysis of sand–geomembrane interactions by capturing the kinematics of particles at the contact plane. Additionally, micro-topographical analysis was carried out using a digital profilometer to measure the surface changes of the geomembranes after shearing. By combining the findings from the μCT of sands and micro-topographical analyses of sheared geomembranes, this study aims to gain insights into the macroscopic shear behavior and relate it to the underlying micro-mechanisms. The findings indicated that the increased shear strength observed in irregular particles has a direct correlation with the deeper indentations caused by these particles and the larger localized shear zones associated with these particles.

Keywords Geomembrane · Fractal dimension · Micro-computed tomography · Non-dilative interface · Digital image correlation · Profilometer

Introduction

The application of geomembranes in combination with soils poses an interesting problem of interaction of soil and polymer at the interface, which plays a crucial role in determining the overall stability and performance of various geotechnical structures, including landfills. Several researchers have categorized geosynthetic interfaces into two groups: "non-dilative" and "dilative", depending on the surface characteristics of the geosynthetic material and related volumetric changes of the reinforced systems during shear [1–3]. Non-dilative interfaces refer to interfaces where soil particles undergo shear with a geosynthetic material, such as a geomembrane, without experiencing any significant volume changes. Interfaces that facilitate volume change during shear are referred to as dilative, such as a geotextile. The current study deals with soil–geomembrane interfaces, which are non-dilative. The load transfer mechanism occurring at non-dilative interfaces is primarily influenced by friction, with no associated changes in volume observed during the process of shearing. The frictional mechanisms encompass the processes of sliding and plowing of the surfaces of the geomembrane due to the presence of granular material. These mechanisms are influenced by factors, such as the shape and the size of the particles [2, 4–8], the magnitude of the normal stress applied [8–13], and the surface characteristics of the continuum material [1, 4, 8, 10, 14]. Markou and Evangelou [8] performed an extensive study on different sand–geomembrane interfaces considering the effect of particle shape and geomembrane surface roughness. They observed that interface shear resistance of sand grains of sub-angular shape and geomembranes with rough surfaces is more compared to that of rounded sand grains and smooth geomembranes. Dove and Frost [4] and Vangla and Latha [5] have demonstrated that the transition from sliding to plowing in frictional mechanisms occurs at a

✉ Gali Madhavi Latha
madhavi@iisc.ac.in

Rizwan Khan
rizwankhan@iisc.ac.in

[1] Department of Civil Engineering, Indian Institute of Science, Bangalore 560012, India

critical normal stress. They have further proposed that, in the case of materials of low hardness such as geomembranes, the frictional behavior at the critical normal stress and beyond is influenced by the micro-level shear-induced surface changes resulting from effective particle contacts within the geomembrane.

Most of the past researches on soil–geosynthetic interface shear response either neglected the particle morphology or used two-dimensional (2D) morphological descriptors computed based on 2D particle projections [15–20]. Most studies considering the 2D particle shape characterizations in literature used photographs of the particles resting on their planes of maximum stability or size. Such measurements have serious limitations since they miss morphological data from all other orientations. Even in studies in which images taken in many orientations were used, the mean shape parameters from 2D image analysis cannot adequately capture the particle shape. Thus, reliable particle morphological quantification requires measurement of 3D shape parameters. Micro-computed tomography (μCT) allows 3D viewing and measurement of geometrical properties of granular materials [21–26].

The occurrence of a highly concentrated shear zone in close proximity to the continuum material is a significant deformation phenomenon at the mesoscale. This phenomenon leads to gradual failure at the interfaces between soil and structures [27–31]. The occurrence of such failures can have significant implications for various soil–reinforcement interfaces. According to Tehrani et al. [32], the shear zone thickness (t_s) varies between 3.9 and 5.2 times the mean particle size (d_{50}) when non-displacement piles are tested in sands of medium to high density. Lashkari and Jamali [30] conducted an investigation of sand–geomembrane interfaces through a series of direct interface tests. Their findings revealed that the t_s/d_{50} values for sand–geomembrane interfaces range from 3.85 to 11.87. Recently, Kandpal and Vangla [2] conducted interface shear tests involving sand–geomembrane and sand–transparent acrylic plate to explore the impact of sand particle morphology and geomembrane hardness on particle kinematics and frictional behavior. They found that angular particles exhibit a greater tendency for translational movement during shear, with very less rotational movement. This behavior was attributed to the increased interlocking ability of angular particles, which promoted higher resistance to rotational motion.

The measurement of shear-induced surface changes of geomembranes provides valuable insights into the microscopic shear mechanisms occurring at the interfaces between sand and geomembranes. Accurate measurement of the changes induced to the surfaces of geomembranes due to the movement of sand particles during shear is possible through profilometry. A correlation between the shear behavior of sand–geomembrane interfaces at a macro-scale and the shear-induced changes to the continuum surface can then be established through visual inspections and quantifications of roughness [2, 5, 33].

This paper deals with the multi-scale shear response of sand–geomembrane interfaces through direct shear experiments and digital image analysis. Micro-computed tomography (μCT) was employed for the acquisition of three-dimensional (3D) images of sand particles, and multiple MATLAB codes were developed to quantify their shape characteristics and surface texture. The kinematics of particles in contact with the geomembrane surfaces was assessed through digital image correlation (DIC) technique. A digital profilometer was used to quantify the micro-level surface changes to geomembrane surfaces resulting from the shearing process with sands, which were correlated to the macroscopic shear response.

Material Description

Two types of graded sands, namely manufactured sand (MS) and river sand (RS), with different shape characteristics and almost similar mean particle size were adopted for this study. Microscopic images and 3D visualization of scanned specimens of sands are shown in Fig. 1. The particle size distribution of both the sands obtained through sieve analysis is shown in Fig. 2. As per the Unified Soil Classification System (USCS), both the sands were classified as poorly graded sands (SP). Index properties of these sands are listed in Table 1.

A smooth geomembrane (GMB) was used as the continuum material in this study. The scanning electron microscopic (SEM) image of the geomembrane specimen along with its surface profile is shown in Fig. 3. The surface profile was obtained using the Bruker's stylus profilometer (DektakXT), and the profile was traced by a stylus tip of 12.5 μm radius for an evaluation length of 8 mm. Table 2 presents the properties of GMB, as given by the manufacturer.

The significance of evaluating the surface topological properties of continuum material has resulted in the formulation of several indices, among which average roughness (R_a) is studied here. The average roughness of a profile is the arithmetic mean of the absolute values of the profile height deviations with respect to the mean line within a specified sampling length. It is calculated by measuring the deviations from the mean line, as indicated in Eq. (1)

$$R_a = \sqrt{\frac{\int_0^l z(x)\mathrm{d}x}{l}}, \tag{1}$$

where $z(x)$ is the profile height at x with respect to the mean line and l is the sampling length. In this study, a stylus profilometer was used to measure the profiles of the

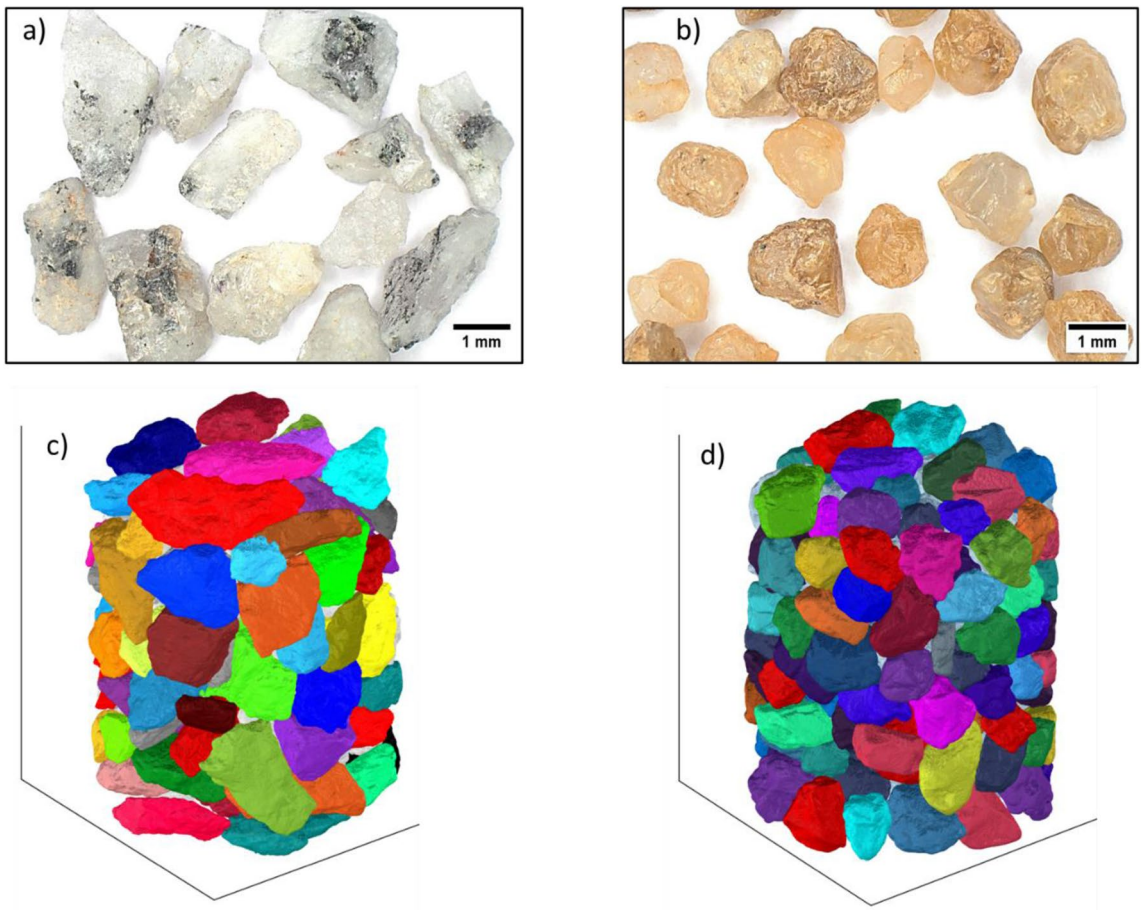

Fig. 1 Microscopic and 3D visualization of sand particles: **a** microscopic image of MS particles; **b** microscopic image of RS particles; **c** µCT image of MS sample; **d** µCT image of RS sample

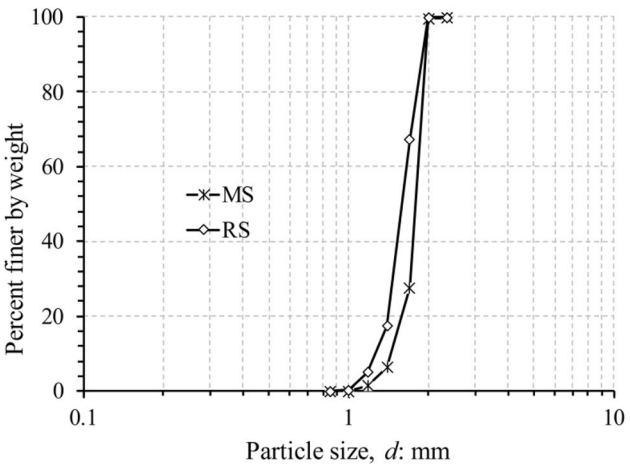

Fig. 2 Grain size distribution of sands

geomembrane surfaces. The profile of the smooth virgin geomembrane (refer to Fig. 3) had an average roughness (R_a) of 4.16 µm with $l = 8$ mm. Several researchers [6, 11, 13, 30, 34, 35] presented substantial experimental evidence to demonstrate the impact of normalized roughness (R_n) on the volume change and frictional characteristics of soil–structure interfaces. Equation (2) gives the normalized roughness (R_n) of geosynthetic materials interfacing with sands with a given mean particle size (d_{50}).

$$R_n = \frac{R_{max}(l = d_{50})}{d_{50}}, \tag{2}$$

Table 1 Index properties of test sands

Property	MS	RS
$d_{50,}$ mm	1.76	1.58
Specific gravity, G_s	2.62	2.67
Coefficient of curvature, C_c	1.12	1.03
Coefficient of uniformity, C_u	1.26	1.31
Minimum void ratio, e_{min}	0.757	0.650
Maximum void ratio, e_{max}	0.956	0.842

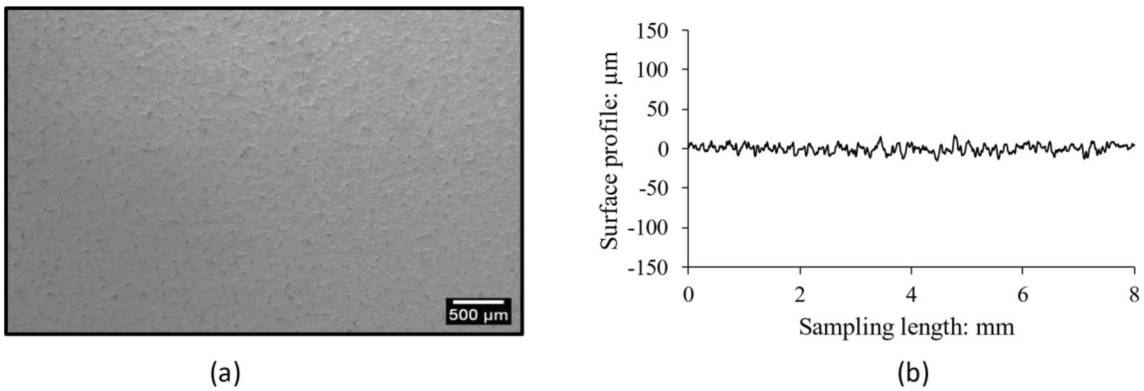

Fig. 3 Surface characterization of the geomembrane: **a** SEM image; **b** surface profile

Table 2 Properties of the geomembrane

Property	Value
Mass per unit area, g/m^2	940
Thickness, mm	1.0
Ultimate tensile strength, kN/m	
Yield	15
Break	27
Elongation, %	
Yield	12
Break	700

where R_{max} represents the maximum difference in height between the lowest valley and the highest peak within a profile, measured over a sampling length (l) equal to d_{50}. For sand–geotextile interfaces, the range of R_n values is between 0.135 and 0.191, while for sand–GMB interfaces, the range is between 0.015 and 0.018 [30]. According to Martinez and Frost [31], when the normalized roughness (R_n) of rough sand–structure interfaces exceeds a threshold of 0.10 to 0.15, the height of the contact surface asperities is significant enough to induce sand dilation, resulting in shear failure. Conversely, when sand encounters smooth structures characterized by low values of normalized roughness ($R_n < 0.03$), the size of the sand particles is larger than the asperities of the surface. Consequently, the primary interaction between the sand particles and the smooth contact surface involves sliding, without significant dilation occurring. In this study, the normalized roughness (R_n) obtained for MS-GMB was 0.014 and for RS-GMB was 0.015, which satisfies the criteria of smooth interfaces.

3D Shape Characterization of Sand Particles

Image Acquisition

The utilization of high-resolution X-ray technology on laboratory specimens enables the µCT technique to facilitate the scanning of objects and acquire three-dimensional images that depict material composition and density through gray values. Each sand sample was scanned using a Bruker µCT (SkyScan 1272). During the rotational movement of an object placed between an X-ray source and a detector, a micro-computed tomography (µCT) scan acquires multiple projections. The volumetric reconstruction software developed by SkyScan, known as *NRecon*, utilizes angular projections obtained from µCT scans to reconstruct the slices of the object with automatic scan geometry adaptation. To enhance the efficiency of the scanning procedure, the sand particles were densely packed within the acrylic tubes measuring 11 mm in diameter and 15 mm in height. The scanning resolution for all samples was set at 10 microns per voxel. To reduce the noise and recover and separate the scanned particles, the µCT images were processed through multiple image processing steps. To start with, the noise in the raw µCT data was reduced by pre-processing the µCT images by applying a 3D median filter, which has a radius of three voxels. The segmentation technique employed in this study is thresholding segmentation, specifically utilizing Otsu's algorithm [36]. This method was utilized to differentiate the sand grains from the void spaces and the boundaries. The binary 3D µCT images were generated using voxel representation in which a voxel value of 1 represented the solid sand particle and a voxel value of 0 represented the background (residual material). The sand particles in contact with each other were separated, and a sequential number was assigned to each particle using a modified version of the 3D watershed segmentation technique described by

Kong and Fonseca [22]. Figure 4 illustrates the sequence of image processing steps adopted in this study.

3D Shape Characterization

The biggest limitation of many earlier studies on sand particle morphology in the context of interface shear response with geosynthetics is that most of the shape characterizations were qualitative [10, 37]. The analysis of shape parameters in these studies was done using the morphological charts developed based on visual evaluation of particle images [38, 39]. Such analysis is time-consuming and subjective in nature. As stated earlier, 2D particle shape indices are extremely sensitive to image orientations and hence they are non-unique and incomplete measurements of particle shape. Therefore, quantification of three-dimensional particle morphology is critical for accurate representation of particle shape.

Sphericity refers to the extent to which a particle's shape is close to a sphere, whereas roundness is a measure of the sharpness of the corners of the particles. The determination of a particle's sphericity in three dimensions requires the calculation of its surface area and volume. This was accomplished through reconstruction of particle geometry using spherical harmonics (SH) analysis. Utilizing the SH reconstructed surface of a particle, a method was developed to determine the necessary surface curvature for the computation of three-dimensional roundness. Utilizing the principal curvatures to quantify the roundness of sand particles allowed the identification and the outlining of potential corners. Typical particles of MS and RS are shown in Fig. 5. Shape parameters were calculated for all particles in the scanned specimens and average values and statistical distribution are presented.

Sphericity (S) was computed as the ratio of the surface area of the sphere of volume equal to that of the particle to the surface area of the particle, using Eq. (3) proposed by Wadell [40].

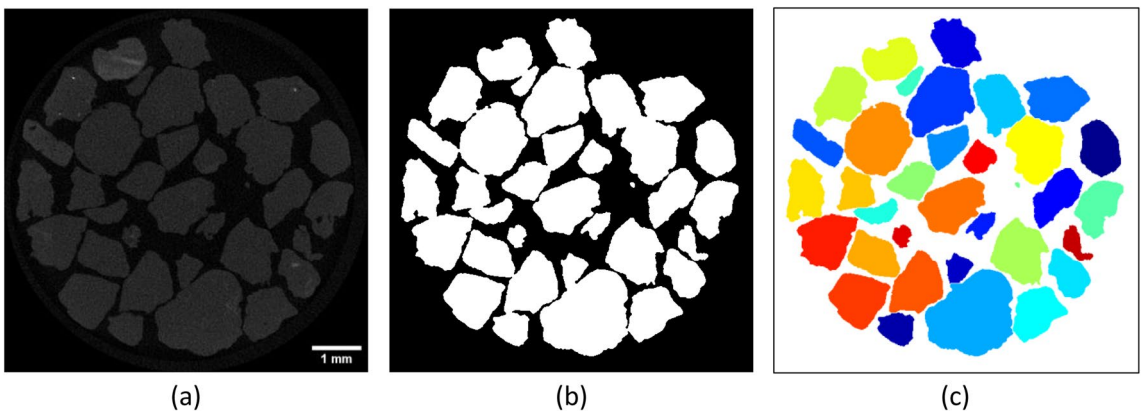

Fig. 4 Sequence of image processing steps **a** μCT image; **b** binary image; **c** image after applying watershed segmentation

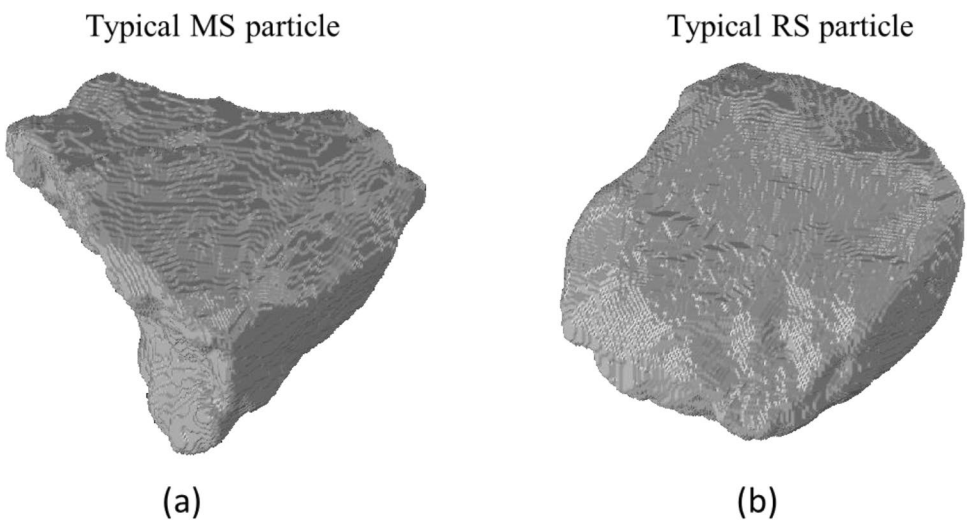

Fig. 5 Micro-CT images of typical MS and RS particles

$$S = \sqrt[3]{36\pi V^2}/\mathrm{SA}, \tag{3}$$

where V and SA are the volume of the particle and the surface area of the particle, respectively.

The 3D roundness (R) is computed as per Eq. (4) proposed by and Zhou et al. [25]

$$R = \frac{\sum c(k)\left|k_{\mathrm{m}}\right|^{-1}}{N r_{\mathrm{ins}}}, \tag{4}$$

where $c(k)$ is a corner coefficient, whose value is 0 for unacceptable corners and 1 for acceptable corners. k_{m} is the mean curvature, N is the number of acceptable corners and r_{ins} is the radius of the largest sphere that can be inscribed within the particle.

Complete description of the methodology used for particle shape reconstruction and computing 3D sphericity and 3D roundness were presented by Khan and Latha [41]. The characterization of the surface texture of the particles was done by defining a fractal dimension for the closed curvilinear boundaries of the sand particles, as explained in the following section.

The surface texture of the natural sand particles can be measured using 3D fractal analysis. Zhou et al. [25] have made significant advances in the quantification of the three-dimensional fractal dimension of sand particles. A novel methodology was developed utilizing the concept of the slit island method (SIM) to compute the three-dimensional fractal dimension of the closed curvilinear boundaries of the sand particles. Nevertheless, the utilization of this technique presents significant challenges and requires substantial computational resources. Additionally, operators must possess a proficient understanding of image processing to successfully implement it. The empirical methodology proposed by Russ [42], Chan [43], and Quevedo et al. [44] requires the utilization of the Fourier power spectrum of 2D gray level images to quantify the fractal dimension. In this study, this approach has been further refined and examined to enhance the precision of fractal dimension within the context of 3D images.

Particle morphology can be efficiently represented through a spherical harmonic (SH) function encompassing a range of spherical harmonic frequencies. The morphological parameters in their respective frequency bands are determined from the amplitudes associated with these frequencies [45]. The amplitude (l_n) corresponding to a spherical harmonic frequency can be calculated using Eq. (5).

$$l_n = \sqrt{\sum_{m=-n}^{n} a_n^m a_n^{m^*}}, \tag{5}$$

where the symbol * represents the conjugate transpose. a_n^m represents the SH coefficients, n and m denote the SH degree and order, respectively and D_n is the spherical harmonic descriptor given by Eq. (6).

$$D_n = \frac{l_n}{l_0} \,(\text{where } n = 2 \ldots .18). \tag{6}$$

The detailed description of SH analysis was introduced in our previous work [41] in which it was found that the parameter l_1 does not have a significant effect on the morphology of the particles. The primary objective of this analysis is to demonstrate the displacement of the reconstructed particle profile relative to the original particle profile using spherical harmonic analysis [46, 47]. The parameter l_0 is a quantitative measure of the particle volume, which is used to normalize the values of l_n to eliminate the effects of particle volume, as shown in Eq. (6). Furthermore, the inclusion of l_1 was disregarded due to its lack of impact on the morphology of the particle reconstructed using spherical harmonics. The present study establishes clear definitions for the spherical harmonic descriptors that can effectively characterize the morphology of particles.

The spherical harmonic descriptor D_n and the spherical harmonic degree n are exponentially correlated, as given in Eq. (7)

$$D_n \propto n^{\beta}, \tag{7}$$

where β is equal to $-2H$, and H represents the Hurst coefficient [43, 44]. The fractal dimension (FD) can be determined if a linear relationship is observed from the graph of the logarithm of D_n versus the logarithm of n, as depicted in Fig. 6. The formula to calculate the fractal dimension is given by Eq. (8).

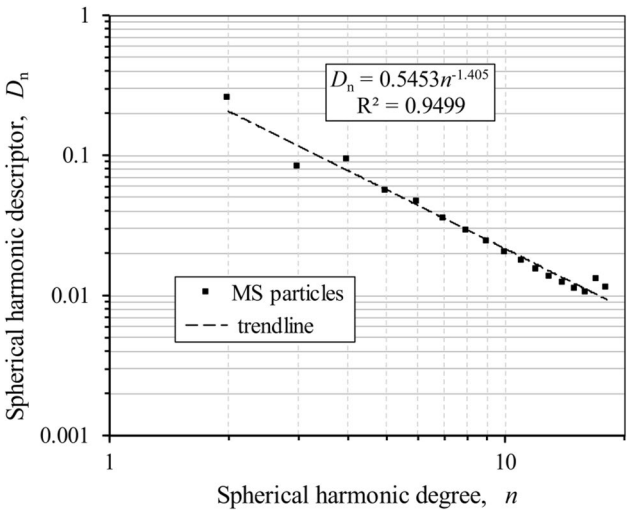

Fig. 6 Relationship between the mean spherical harmonic descriptor and spherical harmonic degree for MS particles

$$FD = \frac{6 + \beta}{2}. \quad (8)$$

The consideration of sphericity as a crucial shape parameter is imperative in the description of three-dimensional particle morphology. Figure 7 displays the cumulative distribution of shape parameters for MS and RS particles. The interdependence of grain shape parameters exhibits a significant level of complexity. While previous research indicated a relationship between sphericity and roundness, with both characteristics tending to increase as grain size increases [48], it is well accepted that developing a mathematical relationship between these two variables is a difficult task. Numerous additional studies have demonstrated that sphericity and roundness are two unique shape descriptors, roundness closely associated with the degree of weathering and sphericity linked to the depositional history [49]. A soil grain has the potential to exhibit a rounded shape without being perfectly spherical, or conversely, it can possess a spherical shape without being perfectly rounded. Nevertheless, it is important to note that relying solely on any individual 3D shape parameter does not provide a comprehensive understanding of the particle's morphology. To fully assess the shape of the grains, it is imperative to quantify their characteristics across various scales. Literature recommends the use of regularity as a descriptor of the overall particle shape, which is calculated as the mean of the shape parameters [50]. The present study examines the particle regularity (ρ) by considering the average of sphericity and roundness, with its reciprocal indicating the particle irregularity. Based on the analysis of the cumulative distribution of shape parameters, it can be observed that MS particles exhibit a lower degree of sphericity and possess a less rounded shape, suggesting that their morphology is characterized by a higher degree of angularity and irregularity compared to the RS particles. When comparing the particles from both specimens, it is observed that most RS particles exhibit sphericity values exceeding 0.8, while most MS particles exhibit sphericity values ranging from 0.6 to 0.8.

The fractal dimension was measured in this study using spherical harmonic-based fractal analysis. Figure 8 displays the histograms and cumulative distributions of the fractal dimension for both RS and MS samples. The findings suggest that the fractal dimension is slightly higher for MS particles compared to that of RS particles, indicating that the surface of the MS particles has a rougher texture compared to that of the RS particles. The mean values and the standard deviation of different morphological descriptors for particles of MS and RS are provided in Table 3.

Interface Direct Shear Tests

Direct shear tests were performed on non-dilative interfaces with the aim of obtaining a deeper understanding of the interactions between sand and smooth geomembrane at various scales. Many researchers have extensively documented the inherent limitations of the conventional direct shear test configuration for soil–geosynthetic interface testing [2, 13, 51]. The present study involves modifying the traditional direct shear configuration by substituting the lower shear box with a 190 mm × 160 mm stiff steel plate. In order to prevent sagging and wrinkling caused by shear stresses, the geomembrane was securely fastened to the steel plate. During the sample preparation process, the top shear box with 80 mm × 80 mm plan dimensions and 44 mm height was firmly fixed to the rigid steel platform using holders. An adjustable shaft was used to enhance the passive resistance, thereby mitigating the risk of tilting and rotation of the shear box during the shearing process. The front side of the shear

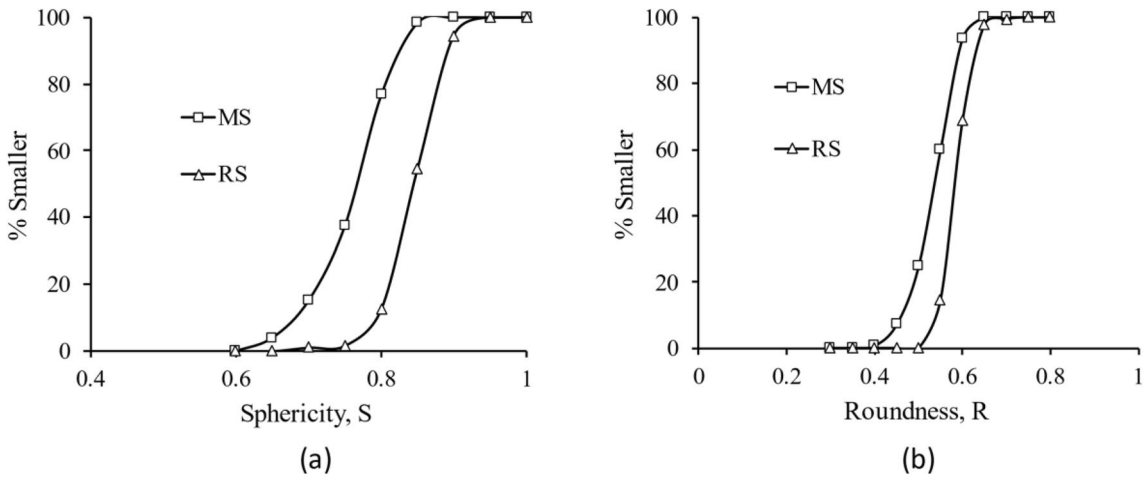

Fig. 7 Cumulative distribution of shape parameters: **a** Sphericity; **b** Roundness

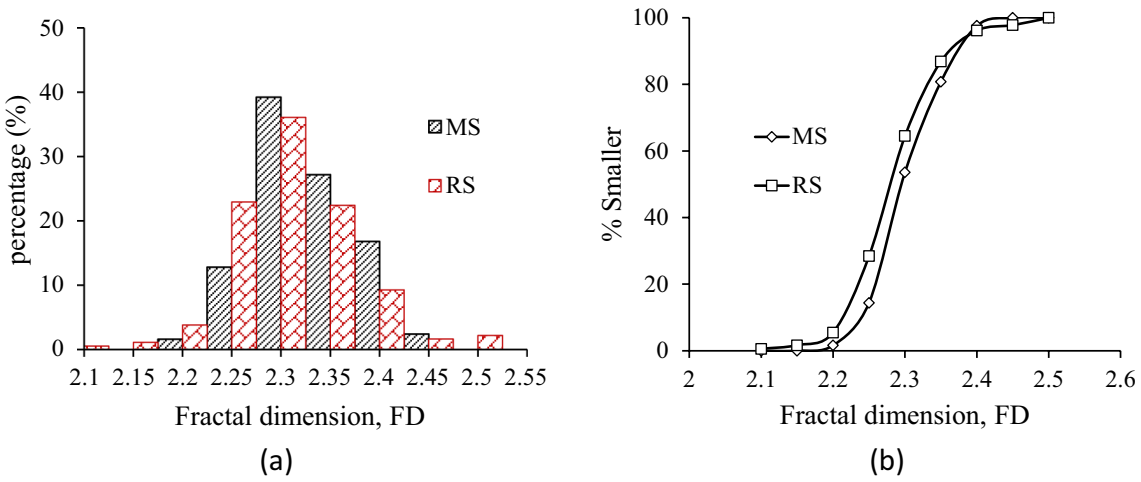

Fig. 8 Variation of fractal dimension of sand particles: **a** Histogram; **b** cumulative distribution

Table 3 Shape descriptors of the tested sand particles

3D shape descriptor	MS		RS	
	Mean value	Standard deviation	Mean value	Standard deviation
Sphericity, S	0.76	0.055	0.84	0.039
Roundness, R	0.53	0.048	0.58	0.033
Regularity, ρ	0.64	0.052	0.71	0.036
Fractal dimension, FD	2.300	0.051	2.283	0.062

box was created using a transparent Perspex sheet to facilitate the observation of particle motion and simplify the process of capturing images for shear band analysis. In all the experiments, the sample preparation involved the sequential filling of the shear box with three uniform layers of dry sand. Subsequently, each of these layers was compacted with a wooden hammer to attain the target relative density (D_r). Prior to shearing, the initial void ratio (e_0) of the specimens was calculated by directly measuring the soil mass and the specimen's height after applying the normal stress, as described by Afzali-Nejad et al. [27]. This produced $e_0 = 0.794$ ($D_r \approx 81\%$) for all MS specimens and $e_0 = 0.688$ ($D_r \approx 80\%$) for all RS specimens. The experiments were carried out at normal stress levels of 40 kPa, 80 kPa, and 120 kPa, with a displacement rate of 1.25 mm/min, concluding a shear displacement of 15 mm, as per ASTM D5321/D5321M-14. While the specimens were sheared, videos of the interface were captured using Olympus OMD-EM-1-Mark-III camera. For the purpose of shear band analysis, high-resolution images were obtained by extracting frames from the recorded videos at different displacement intervals. Figure 9 presents a photographic representation of the experimental arrangement employed for the purpose of video recording during the course of the experiment.

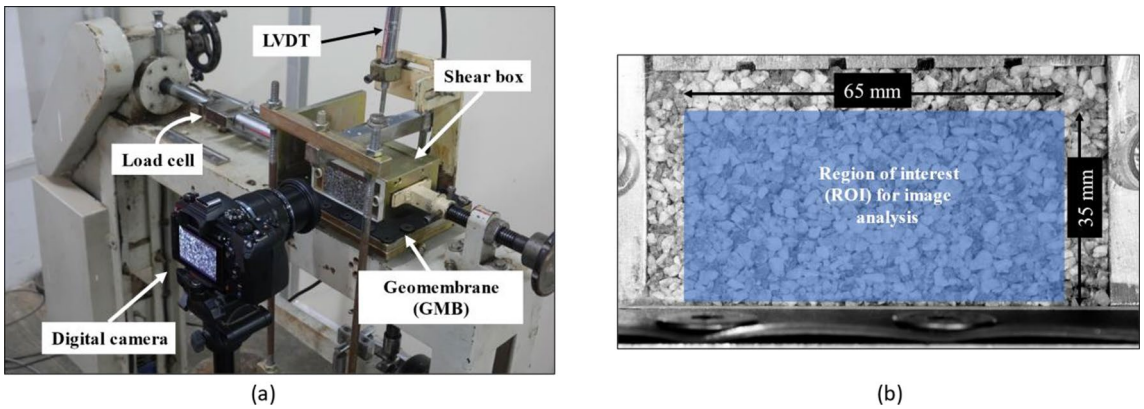

Fig. 9 Experimental set-up used in this study: **a** video capturing arrangement; **b** close up view of the shear box with the Region of Interest (ROI) marked

Digital Image Correlation (DIC) Analysis

The analysis of shear bands, which are associated with the concentrated deformation of granular materials, carries substantial significance in various fields including materials science, mechanics, industrial engineering, hydraulic engineering, and civil engineering. The present study employs the Digital Image Correlation (DIC) technique to determine the localized thickness of shear zones in experiments conducted on the sand–geomembrane interfaces. The DIC analysis was conducted in MATLAB using the open-source software "Ncorr", which was developed by Blaber et al. [52]. The particle kinematic behavior at the interface was recorded using the Olympus OMD-EM-1-Mark-III camera, which was placed at a distance of 18 cm from the transparent side of the shear box. Throughout the shearing procedure, high-definition videos were captured at a 4 k resolution (3840 pixels × 2160 pixels) and at 30 frames/s, equating to an approximate magnification of 0.023 mm per pixel. An additional light source was used to improve the degree of illumination, thereby enhancing the visual clarity of the resultant images. The Ncorr software offers a circular subset for image analysis. In this study, the radius of the subset was set to 90 pixels, with a spacing of 10 pixels between each consecutive measurement point.

Micro-Topographical Analysis of Sheared Geomembranes

The importance of quantifying the surface roughness of the geosynthetic materials in their virgin and sheared states for establishing precise interface shear mechanisms is well-understood by the researchers in recent years [1, 3, 5, 7, 15, 29, 33, 53]. This interest originates from the measurement of surface topographical characteristics associated with these materials. Figure 10 depicts the changes to the surface of typical geomembrane samples caused by shear stress, as observed through microscopic images.

Stylus profilometry, optical profile microscopy (OPM), atomic force microscopy (AFM), and non-contact optical profilometry are commonly employed techniques for evaluating the surface roughness of sheared geomembranes. The utilization of contact-based stylus profilometers limits the surface profile acquired during the traversal of the stylus profiler tip to two-dimensional (2D) data. The OPM method measures the roughness by measuring three cross sections positioned at an angular orientation of 120° relative to one another. However, it should be noted that this approach is both time-consuming and lacks comprehensiveness. In their study, Dove and Frost [7] utilized atomic force microscopy (AFM), a technique characterized by a limited scanning area and applicability restricted to a specific range of geomembranes. Among the various approaches that have been discussed here, the optical profilometer stands out as the most advanced tool. Non-contact image-based profilometry is utilized to collect comprehensive data on small regions, which may then be integrated to assess the overall roughness of a surface. Nevertheless, this technique necessitates the use of surfaces that possess a high degree of reflectivity in order to achieve images that exhibit adequate levels of contrast. In a recent study conducted by Vangla and Latha [33], optical profilometry was utilized to determine the changes occurring on geomembrane surfaces as a result of shear forces. To improve the reflectance characteristics, a thin coating of gold was applied onto the samples of geomembrane. The gold coating, however thin it is, can induce error into the surface roughness measurements. In the current study, surface roughness of the geomembrane specimens was measured using Bruker's stylus profilometer DektakXT. The study involved tracing 160 surface profiles for each sample using a stylus tip with a radius of 12.5 µm and a resolution of 4 µm per point. The profilometer used a 3D map option to

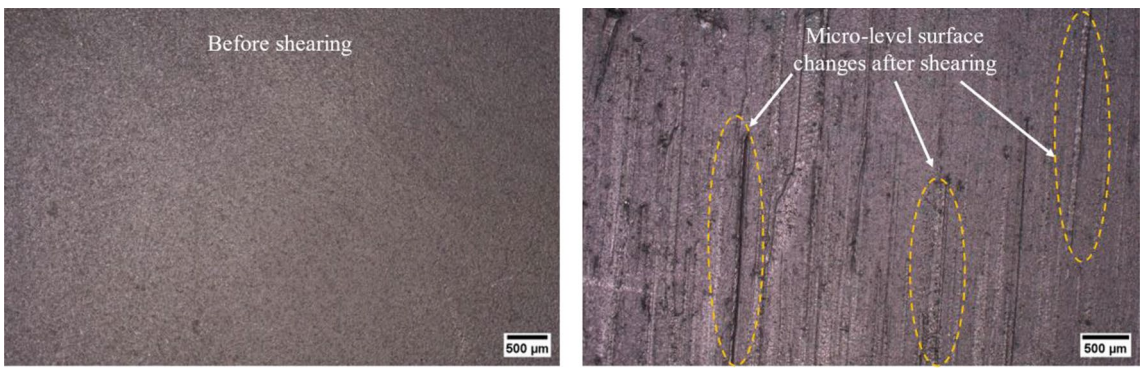

Fig. 10 Microscopic images of geomembrane surface: **a** before shearing; **b** after shearing against MS particles at a normal stress of 120 kPa

automatically gather extensive data on the surface roughness of the geomembrane to create the 3D surface profiles of the geomembranes.

Results and Discussion

The shear stress and the shear displacement measured from interface shear tests conducted at different normal stresses are shown in Fig. 11. The interfaces exhibited an elastic-perfectly plastic shear behavior. Since the surface asperities of the geomembrane are significantly smaller in size compared to the sand particles, the surface can be treated as a smooth surface, which causes peak and residual shear stresses to be almost equal at all normal stresses. These interfaces are non-dilative since negligible volume change was seen during shearing. The peak shear strength is noted to be higher for MS–GMB interfaces because MS particles are relatively more irregular and rougher. The peak angle of friction observed for MS–GMB interfaces was approximately 33% more than that observed for RS-GMB interfaces.

Figure 12 illustrates the relationship between normal stress and interface friction coefficient (μ). Interface friction coefficient is defined as $\mu = \tan(\delta_p)$ where δ_p is the peak friction angle. The observed trend indicates a decrease in the friction coefficient with an increase in the normal stress till a point denoted as the critical normal stress, followed by an increase [2, 4]. Roberts [54] offers a comprehensive explanation to the decrease in the interfacial friction coefficient of bulk solids at higher normal stresses. The shape of the yield locus in solids is convex upward, thus intersecting with the shear stress axis at a point corresponding to the internal friction angle of the sand. Furthermore, an increase in the normal stress initially leads to a decrease in the friction angle due to the characteristics of the yield locus and leads to the formation of more pronounced grooves on the surface of the geomembrane. When the normal stress reaches the critical value, the interaction of sand particles with the geomembrane, which is mainly sliding at lower

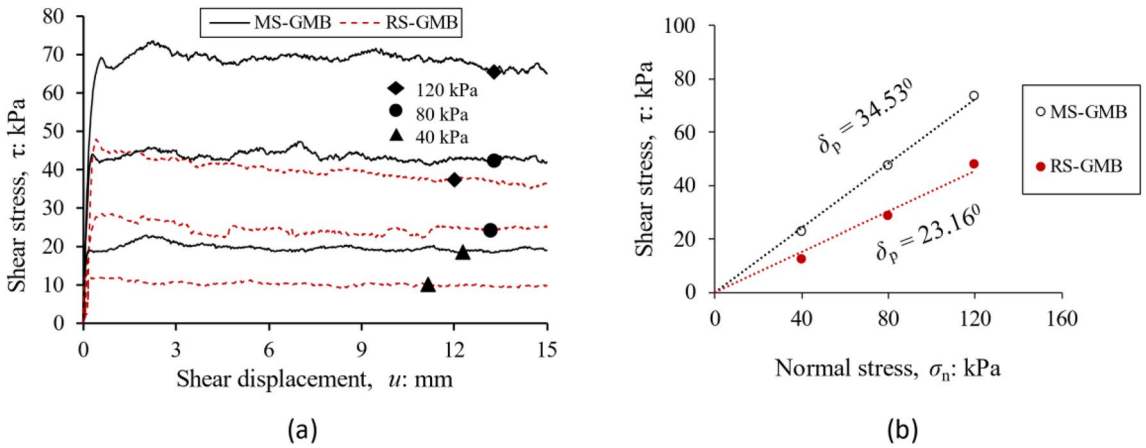

Fig. 11 Behavior of sand–geomembrane interfaces in direct shear: **a** stress–displacement response; **b** peak shear stress envelopes

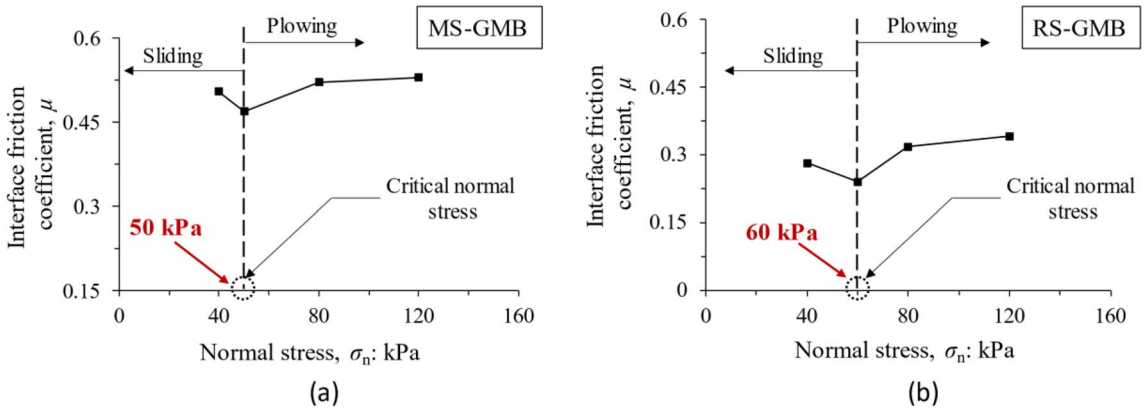

Fig. 12 Transformation of shearing mechanisms and critical normal stress: **a** MS–GMB interface; **b** RS–GMB interface

normal stresses, transforms into plowing at higher normal stresses. Consequently, this transition resulted in an increase of the interface friction coefficient, as depicted in Fig. 12. The hardness of the continuum material and the shape of the particles primarily govern these changes to the friction coefficient [2]. Considering the influence of particle shape, the MS particles, characterized by their increased angularity and surface texture, demonstrated higher shear stress and friction coefficient in comparison to the RS particles. In order to evaluate the critical normal stress, few additional tests were conducted at normal stress levels of 50 kPa and 60 kPa, and the results are presented in Fig. 12. This study indicates that the critical normal stress is 50 kPa for MS–GMB interfaces and 60 kPa for RS–GMB interfaces as shown in Fig. 12a, b, respectively. The reason for the lower critical normal stress in MS–GMB interfaces is attributed to the more pronounced grooves caused by their sharp edges, even at reduced normal stresses. This shift in turn leads to an earlier initiation of the plowing mechanism at lower normal stresses in MS interfaces, confirming the observations from similar studies reported earlier [2, 4, 5].

Additionally, in order to obtain a deeper understanding of the shearing mechanism and the impact of normal stress on the friction coefficient at the interface, the deformation of particles at the interface was examined using Digital Image Correlation (DIC) analysis. Figure 13 illustrates the variation of the shear strain field at a normal stress of 120 kPa, obtained at the limiting shear displacement of 15 mm. The plot clearly shows a zone of intense shear strain near the interface, which diminished after a certain vertical distance. In a typical plot depicting the variation of shear strain with vertical distance shown in Fig. 13b, the thickness of the shear zone (t_s) is measured as the vertical distance above the interface within which the shear strains are visualized. The plots of variation of shear strain with vertical distance at different normal stresses for sand–GMB interfaces are shown in Fig. 14 and the measured valued of t_s for these interfaces are presented in Table 4. It can be seen that the thickness of the localized shear zone decreases at higher normal stresses due to increased confinement effect, which limits the deformation behavior of the sample. The value of t_s/d_{50} varied from 4.26 to 4.66 for MS–GMB interfaces and 3.67 to 4.11 for RS–GMB interfaces. The particle kinematics observed at the interface were further supported by the measured surface changes induced by shear in the tested geomembranes. In addition, it can be observed from Fig. 14 and Table 4 that the localized shear zone is thicker for MS–GMB interfaces in comparison to RS–GMB interfaces. The reduced interaction between particle asperities and the surface of the geomembrane can be attributed to the lower fractal dimension, or surface roughness, of RS particles. This leads to a decrease in the force generated, because of which the rotational movement of particles at the interface gets restricted. This observation provides conclusive evidence that the shear force generated at the interface governs the kinematics of the particles at the interface.

After finishing the interface shear tests, the geomembrane specimens were removed and the central parts of the specimens which displayed the most pronounced surface abrasion were carefully cut for surface analyses. As anticipated, geomembrane surfaces exhibited greater wear when subjected to shear stresses from MS particles as opposed to RS particles. This can be primarily attributed to the higher irregularity and complex surface texture of the MS particles. The surface height maps for both the original geomembrane and the geomembranes subjected to shearing under a 120 kPa normal stress are depicted in Fig. 15. As explained earlier, these 3D surface profiles were constructed using multiple 2D

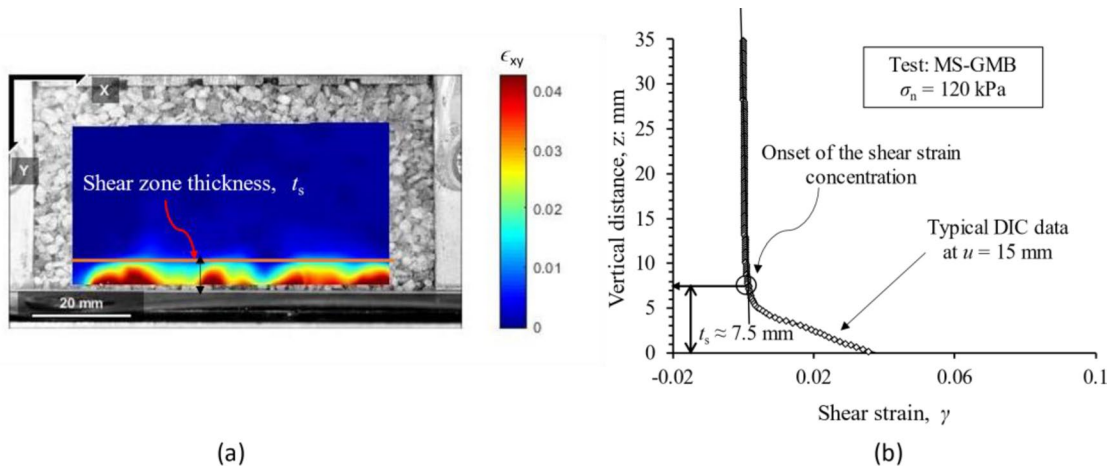

Fig. 13 Strain localization and shear zone evolution at the sand–geomembrane interface: **a** shear strain field; **b** shear strain variation along the vertical distance of ROI

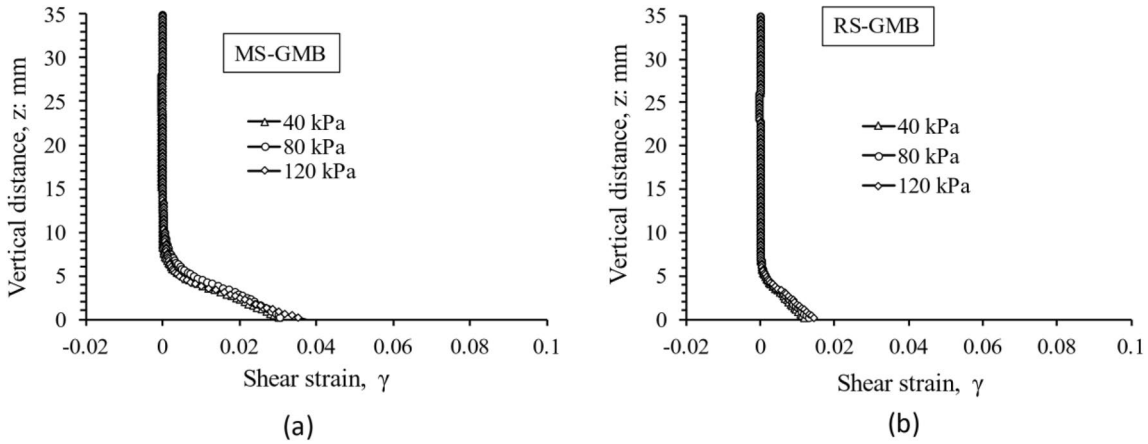

Fig. 14 Shear strain variation along the vertical distance of ROI for sand–geomembrane interfaces

Table 4 Thickness of localized shear zone measured for different sand-geomembrane interfaces

Interface	Normal stress, σ_n, kPa	Thickness of the localized shear zone	
		t_s, mm	t_s/d_{50}
MS–GMB	40, 80, 120	8.2, 7.9, 7.5	4.7, 4.5, 4.3
RS–GMB	40, 80, 120	6.5, 6.3, 5.8	4.1, 4.0, 3.7

surface profile measurements made using the contact profilometer. Comparisons showed that tested geomembranes showed clear tracks of sand particle plowing, the depth and the width of these tracks being significantly higher for MS particles. In Fig. 15c, a highly pronounced groove is visible, and this groove has been formed due to the shearing action of a very sharp edge of the MS particle on the geomembrane surface. The roughness parameters were computed by analyzing the

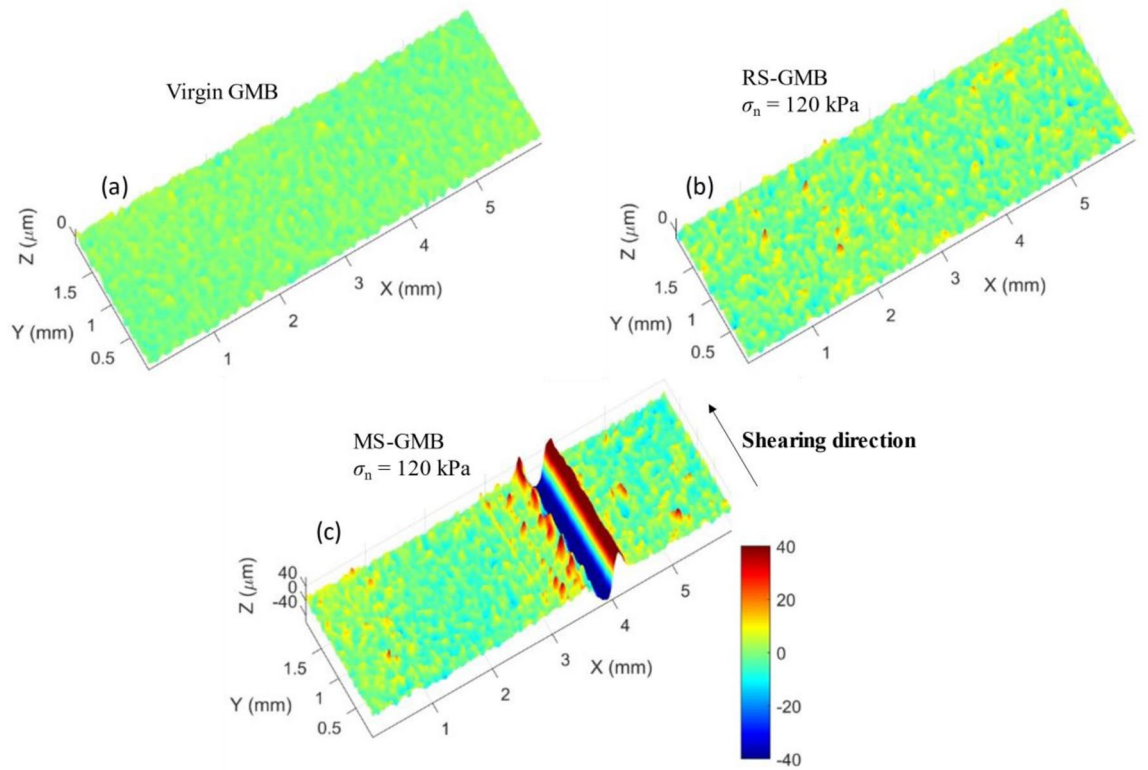

Fig. 15 Typical images showing the micro-topography of geomembrane specimens: **a** virgin GMB; **b** GMB sheared against RS particles at 120 kPa; **c** GMB sheared against MS particles at 120 kPa

profiles of surface heights for virgin and tested geomembrane surfaces. The three different roughness parameters, namely average roughness (S_a), root mean square roughness (S_q), and the greatest peak to valley height (S_z), measured for the virgin and tested geomembranes are presented in Table 5.

As observed in Table 5, the S_z parameter showed an increase with the increase in normal stress magnitude and the irregularity of the sand grains, indicating that the presence of sharp corners on the MS particles caused more abrasion on the geomembrane surface, leading to deeper indentations. In addition, the surface roughness parameters S_q and S_a of the geomembrane samples sheared by MS particles were greater than those of the samples sheared by RS particles, suggesting that the MS particles resulted in a rougher geomembrane surface compared to the RS particles. The difference in roughness increased nonlinearly with the increase in the normal stress, because of the deeper indentations of sand particles. For example, the additional average surface roughness of the geomembrane tested with MS at 40 kPa normal stress compared to the virgin geomembrane is 1.8 times to the corresponding value for RS and it increased to 2.6 times and 4.9 times, respectively at 80 kPa and 120 kPa. Surface roughness ratio, which is the ratio of the additional roughness imparted to the geomembrane by shearing with MS particles to that imparted by RS particles, measured in terms of S_a, S_q and S_z is plotted in Fig. 16. While all roughness ratios increased with the normal stress, the variation is substantially visible for S_q, because of its composition. The 33% higher peak interface friction angle for GMB–MS interfaces is a result of this increased roughness, which increases particle interlocking with the surface asperities, thereby offering higher resistance to shear. The higher shear resistance of MS interfaces was evident through thicker local shear zone observed in the tests. All these observations and correlations suggest that the higher interface shear strength derived from MS particles can be directly linked to the highly irregular shape of these particles.

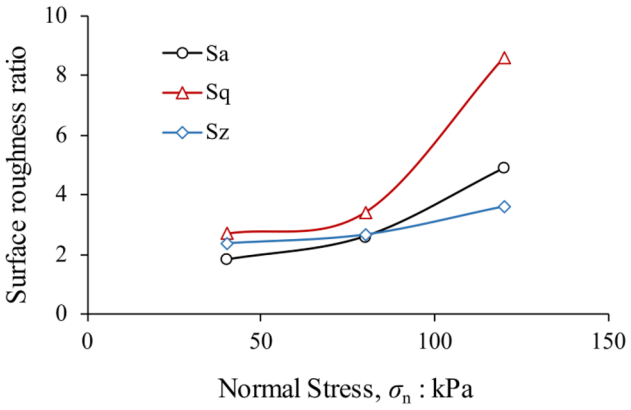

Fig. 16 Variation of roughness ratios with the normal stress

Conclusions

The objective of this study is to investigate the quantitative influence of particle shape and normal stress levels on the shear response of non-dilative interface systems across different length scales to establish meaningful correlations between shear interactions at a micro-scale and the frictional response at a macro-scale. To achieve this objective, X-ray micro-CT is utilized for the characterization of particle shape in three dimensions. Digital Image Correlation (DIC) analysis is employed to investigate the localized deformation of sand occurring at the interfaces between sand and geomembranes. In addition, micro-topographical analysis is performed on virgin and tested geomembranes using a digital profiler. Following major conclusions can be drawn from this study:

a) The effect of particle shape on the multi-scale shear behavior of non-dilative interfaces is evident. MS particles have higher interlocking tendency derived from their highly irregular particle shape and rougher surface texture, which is the reason for the higher interface shear resistance exhibited by them as compared to RS particles. The sharper edges of MS particles caused deeper grooves on geomembrane surfaces after shearing, which resulted in 33% higher peak friction angle of the MS interfaces compared to RS interfaces.
b) The effects of normal stress levels on the interface friction can be correlated to the shear strain localization at the interface coupled with micro-level shear-induced changes to geomembrane surfaces. With the increase in the normal stress, the friction coefficient initially decreased and then increased due to the transformation of shearing mechanism from sliding along the interface to plowing through the geomembrane surface. The localized shear zones are observed to shrink at higher normal stress levels due to the increased confinement effect.
c) Thickness of the localized shear zone (t_s) is higher for irregular particles due to their ability to cause deeper grooves on the geomembrane surface, resulting in a

Table 5 Surface roughness parameters of geomembrane specimens in their virgin and sheared states

GMB type	Normal stress, σ_n, kPa	S_a (μm)	S_q (μm)	S_z (μm)
Virgin	–	2.04	2.85	24.11
Tested with MS	40, 80, 120	3.75, 4.69, 7.6	5.45, 6.61, 13.75	64.18, 92.49, 122.18
Tested with RS	40, 80, 120	2.98, 3.06, 3.18	3.81, 3.95, 4.12	41.05, 49.77, 51.16

thicker zone of intense shear deformations. The t_s/d_{50} ratios varied from 4.3 to 4.7 for MS–GMB interfaces and 3.7 to 4.1 for RS–GMB interfaces.

d) Surface roughness ratio, which is the ratio of the additional roughness induced by shearing a geomembrane with MS particles to the corresponding value with RS particles, is about 2 at a lower normal stress of 40 kPa, and it increased nonlinearly with the normal stress, the effect being more prominent for the root mean square roughness.

Acknowledgements The computing resources utilized in this study were acquired through the DRIP grant provided by the Department of Civil Engineering at the Indian Institute of Science. Authors are grateful to the Ministry of Water Resources, India for this financial support.

Author Contributions Methodology, formal investigation and analysis, conceptualization, parameters formulation and results—review, writing—original draft preparation: RK; ideation, design of experiments, writing—review and editing, supervision: GML.

Data Availability The data generated/analyzed during the study are available from the corresponding author on reasonable request.

Declarations

Conflict of interest The authors declare no conflict of interest.

References

1. Dove JE, Bents DD, Wang J, Gao B (2006) Particle-scale surface interactions of non-dilative interface systems. Geotext Geomembranes 24:156–168. https://doi.org/10.1016/j.geotexmem.2006.01.002
2. Kandpal L, Vangla P (2023) New insights into geotribology of non-dilative interfaces from novel experimental studies. Geosynth Int. https://doi.org/10.1680/jgein.23.00013
3. Dove JE, Jarrett JB (2002) Behavior of dilative sand interfaces in a geotribology framework. J Geotech Geoenviron Eng 128:25–37. https://doi.org/10.1061/(ASCE)1090-0241(2002)128:1(25)
4. Dove JE, Frost JD (1999) Peak friction behavior of smooth geomembrane-particle interfaces. J Geotech Geoenviron Eng 125:544–555. https://doi.org/10.1061/(ASCE)1090-0241(1999)125:7(544)
5. Vangla P, Latha GM (2016) Shear behavior of sand-smooth geomembrane interfaces through micro-topographical analysis. Geotext Geomembranes 44:592–603. https://doi.org/10.1016/j.geotexmem.2016.04.001
6. Uesugi M, Kishida H (1986) Influential factors of friction between steel and dry sands. Soils Found 26:33–46. https://doi.org/10.3208/SANDF1972.26.2_33
7. Dove JE, Frost JD (1996) A method for measuring geomembrane surface roughness. Geosynth Int 3:369–392. https://doi.org/10.1680/gein.3.0067
8. Markou IN, Evangelou ED (2018) Shear resistance characteristics of soil-geomembrane interfaces. Int J Geosynth Gr Eng 4:1–16. https://doi.org/10.1007/s40891-018-0146-6
9. Jewell RA, Wroth CP (1987) Direct shear tests on reinforced sand. Geotechnique 37:53–68
10. O'Rourke TD, Druschel SJ, Netravali AN (1990) Shear strength characteristics of sand-polymer interfaces. J Geotech Eng 116:451–469. https://doi.org/10.1061/(ASCE)0733-9410(1990)116:3(451)
11. DeJong JT, Westgate ZJ (2009) Role of initial state, material properties, and confinement condition on local and global soil-structure interface behavior. J Geotech Geoenviron Eng 135:1646–1660. https://doi.org/10.1061/(asce)1090-0241(2009)135:11(1646)
12. Islam MN, Siddika A, Hossain MB et al (2011) Effect of particle size on the shear strength behaviour of sands. Aust Geomech J 46:85–95
13. Vangla P, Latha GM (2016) Effect of particle size of sand and surface asperities of reinforcement on their interface shear behaviour. Geotext Geomembranes 44:254–268. https://doi.org/10.1016/j.geotexmem.2015.11.002
14. Punetha P, Mohanty P, Samanta M (2017) Microstructural investigation on mechanical behavior of soil-geosynthetic interface in direct shear test. Geotext Geomembranes 45:197–210. https://doi.org/10.1016/j.geotexmem.2017.02.001
15. Alshibli KA, Alsaleh MI (2004) Characterizing surface roughness and shape of sands using digital microscopy. J Comput Civ Eng 18:36–45. https://doi.org/10.1061/(ASCE)0887-3801(2004)18:1(36)
16. Altuhafi F, O'Sullivan C, Cavarretta I (2013) Analysis of an image-based method to quantify the size and shape of sand particles. J Geotech Geoenviron Eng 139:1290–1307. https://doi.org/10.1061/(ASCE)GT.1943-5606.0000855
17. Mora CF, Kwan AKH (2000) Sphericity, shape factor, and convexity measurement of coarse aggregate for concrete using digital image processing. Cem Concr Res 30:351–358. https://doi.org/10.1016/S0008-8846(99)00259-8
18. Pillai AG, Latha GM (2022) Role of particle shape on the shear strength of sand-GCL interfaces under dry and wet conditions. Geotext Geomembranes 50:262–281. https://doi.org/10.1016/j.geotexmem.2021.11.004
19. Sukumaran B, Ashmawy AK (2001) Quantitative characterisation of the geometry of discrete particles. Géotechnique 51:619–627. https://doi.org/10.1680/geot.51.7.619.51393
20. Vangla P, Roy N, Latha GM (2018) Image based shape characterization of granular materials and its effect on kinematics of particle motion. Granul Matter 20:1–19. https://doi.org/10.1007/s10035-017-0776-8
21. Alshibli KA, Druckrey AM, Al-Raoush RI et al (2015) Quantifying morphology of sands using 3D imaging. J Mater Civ Eng 27:1–10. https://doi.org/10.1061/(asce)mt.1943-5533.0001246
22. Kong D, Fonseca J (2018) Quantification of the morphology of shelly carbonate sands using 3D images. Geotechnique 68:249–261. https://doi.org/10.1680/jgeot.16.P.278
23. Fonseca J, O'Sullivan C, Coop MR, Lee PD (2012) Non-invasive characterization of particle morphology of natural sands. Soils Found 52:712–722. https://doi.org/10.1016/j.sandf.2012.07.011
24. Su D, Yan WM (2018) 3D characterization of general-shape sand particles using microfocus X-ray computed tomography and spherical harmonic functions, and particle regeneration using multivariate random vector. Powder Technol 323:8–23. https://doi.org/10.1016/J.POWTEC.2017.09.030
25. Zhou B, Wang J, Wang H (2018) Three-dimensional sphericity, roundness and fractal dimension of sand particles. Geotechnique 68:18–30. https://doi.org/10.1680/jgeot.16.P.207
26. Zhao B, Wang J (2016) 3D quantitative shape analysis on form, roundness, and compactness with μCT. Powder Technol 291:262–275. https://doi.org/10.1016/j.powtec.2015.12.029
27. Afzali-Nejad A, Lashkari A, Shourijeh PT (2017) Influence of particle shape on the shear strength and dilation of sand-woven

geotextile interfaces. Geotext Geomembranes 45:54–66. https://doi.org/10.1016/j.geotexmem.2016.07.005
28. Dejong JT, White DJ, Randolph MF (2006) Microscale observation and modeling of soil-structure interface behavior using particle image velocimetry. Soils Found 46:15–28. https://doi.org/10.3208/SANDF.46.15
29. Frost JD, Kim D, Lee SW (2012) Microscale geomembrane-granular material interactions. KSCE J Civ Eng 16:79–92. https://doi.org/10.1007/s12205-012-1476-x
30. Lashkari A, Jamali V (2021) Global and local sand–geosynthetic interface behaviour. Geotechnique 71:346–367. https://doi.org/10.1680/jgeot.19.P.109
31. Martinez A, Frost JD (2017) The influence of surface roughness form on the strength of sand-structure interfaces. Geotech Lett 7:104–111. https://doi.org/10.1680/jgele.16.00169
32. Tehrani FS, Han F, Salgado R et al (2016) Effect of surface roughness on the shaft resistance of non-displacement piles embedded in sand. Geotechnique 66:386–400. https://doi.org/10.1680/jgeot.15.P.007
33. Vangla P, Latha GM (2017) Surface topographical analysis of geomembranes and sands using a 3D optical profilometer. Geosynth Int 24:151–166
34. Vangla P, Latha GM (2015) Influence of particle size on the friction and interfacial shear strength of sands of similar morphology. Int J Geosynth Gr Eng 1:1–6. https://doi.org/10.1007/s40891-014-0008-9
35. Martinez A, Frost JD, Hebeler GL (2015) Experimental study of shear zones formed at sand/steel interfaces in axial and torsional axisymmetric tests. Geotech Test J 38:409–426. https://doi.org/10.1520/GTJ20140266
36. Otsu N (1979) A threshold selection method from gray-level histograms. IEEE Trans Syst Man Cybern 9:62–66
37. Anubhav, Basudhar PK (2013) Interface behavior of woven geotextile with rounded and angular particle sand. J Mater Civ Eng 25:1970–1974. https://doi.org/10.1061/(asce)mt.1943-5533.0000774
38. Powers MC (1953) A new roundness scale for sedimentary particles. J Sediment Petrol 23:117–119
39. Krumbein WC, Sloss LL (1963) Stratigraphy and sedimentation, 2nd edn. San Francisco, CA, USA
40. Wadell H (1935) Volume, shape, and roundness of quartz particles. J Geol 43:250–280
41. Khan R, Latha GM (2023) Multi-scale understanding of sand-geosynthetic interface shear response through Micro-CT and shear band analysis. Geotext Geomembranes 51:437–453. https://doi.org/10.1016/j.geotexmem.2023.01.006
42. Russ J (1994) Fractal surfaces, 1st edn. Plenum Press, New York
43. Chan KL (1995) Quantitative characterization of electron micrograph image using fractal feature. IEEE Trans Biomed Eng 42:1033–1037
44. Quevedo R, Mendoza F, Aguilera JM et al (2008) Determination of senescent spotting in banana (Musa cavendish) using fractal texture Fourier image. J Food Eng 84:509–515. https://doi.org/10.1016/J.JFOODENG.2007.06.013
45. Kazhdan M, Funkhouser T, Rusinkiewicz S (2003) Rotation invariant spherical harmonic representation of 3D shape descriptors. Eurographics Symp Geom Process 43:156–164
46. Zhou B, Wang J (2017) Generation of a realistic 3D sand assembly using X-ray micro-computed tomography and spherical harmonic-based principal component analysis. Int J Numer Anal Methods Geomech 41:93–109. https://doi.org/10.1002/nag.2548
47. Sun Q, Zheng J (2021) Realistic soil particle generation based on limited morphological information by probability-based spherical harmonics. Comput Part Mech 8:215–235. https://doi.org/10.1007/s40571-020-00325-6
48. EL Fishawi NM (1984) Roundness and sphericity of the delta coastal sands. Acta Mineral Szeged 16:235–245
49. Pettijohn FJ (2004) Sedimentary rocks. CBS Publishers, New Delhi
50. Cho G-C, Dodds J, Santamarina JC (2006) Particle shape effects on packing density, stiffness, and strength: natural and crushed sands. J Geotech Geoenviron Eng 132:591–602. https://doi.org/10.1061/(asce)1090-0241(2006)132:5(591)
51. Lee KM, Manjunath VR (2000) Soil-geotextile interface friction by direct shear tests. Can Geotech J 37:238–252. https://doi.org/10.1139/T99-124
52. Blaber J, Adair B, Antoniou A (2015) Ncorr: open-source 2D digital image correlation Matlab software. Exp Mech 55:1105–1122. https://doi.org/10.1007/s11340-015-0009-1
53. Araújo GLS, Sánchez NP, Palmeira EM, de Almeida das MGG (2022) Influence of micro and macroroughness of geomembrane surfaces on soil-geomembrane and geotextile-geomembrane interface strength. Geotext Geomembranes 50:751–763. https://doi.org/10.1016/j.geotexmem.2022.03.015
54. Roberts AW (2001) Chute design considerations for feeding and transfer. In: Proceedings of BELTON, International materials handling conference. vol. 11, Johannesburg, South Africa